One-pot preparation of iron/alumina catalyst for the efficient growth of vertically-aligned carbon nanotube forests

Arthur Roussey,[a,f] Nicolas Venier,[a] Hussein Fneich,[b] Lucas Giardella,[c] Thomas Pinaud,[b] Saïd Tahir,[c] Mario Pelaez-Fernandez,[d] Raul Arenal,[d,e,g] Ahmad Mehdi [b] and Vincent Jourdain[c,*]

[a] Global Technologies, 496 avenue Francis Perrin, Rousset, France

[b] Institut Charles Gerhardt, UMR5253 CNRS, ENSCM, Université Montpellier, Place Eugène Bataillon, 34095 Montpellier Cedex 05, France

[c] Laboratoire Charles Coulomb, CNRS, Univ. Montpellier, Montpellier, France

[d] Laboratorio de Microscopias Avanzadas (LMA), Instituto de Nanociencia de Aragon (INA), Universidad de Zaragoza, C/ Mariano Esquilor s/n 50018 Zaragoza, Spain

[e] ARAID Foundation, 50018 Zaragoza, Spain

[f] Present address: Grenoble Alpes University, CEA-LITEN, 17 rue des Martyrs, 38054 Grenoble Cedex 09, France

[g] Instituto de Ciencias de Materiales de Aragon, CSIC-U. de Zaragoza, Calle Pedro Cerbuna 12, 50009 Zaragoza, Spain

* Corresponding author: E-mail: vincent.jourdain@umontpellier.fr (V. Jourdain)

Highlights:

- One-pot, simple and fully wet method to prepare catalyst layers for the growth of VA-CNT arrays.
- Nanotube height, diameter distribution, and crystalline quality comparable to those of existing but more costly and less versatile methods.
- The mechanism involves the concomitant formation of an aluminum-based buffer layer from aluminum hydroxides, and of catalyst nanoparticles from iron hydroxides at its surface.

Abstract

The catalytic growth of vertically-aligned carbon nanotubes (VA-CNTs) forest usually requires thin catalyst films deposited by multi-step and costly physical vapor deposition techniques. Here, we demonstrate that an efficient catalyst and its supporting layer for VACNT growth can be prepared by using a simple solution of $Fe(NO_3)_3$ and $Al(NO_3)_3$ deposited on silica in a single step. This process being much simpler and cheaper than existing preparation methods, it can easily be transferred to industry for the low-cost, thin and large-area coating of catalyst for VA-CNT growth. Our study shows that aluminum hydroxides preferentially react with the SiO_2 surface while iron hydroxides tend to form oxide or hydroxide nanoparticles, thus allowing preparation of an aluminum-based buffer layer with iron-based nanoparticles at its surface. Optimization of the Fe/Al ratio and salt concentrations yielded catalysts with performances similar to standard Fe/Al_2O_3 catalysts prepared by physical vapor deposition.

Graphical Abstract

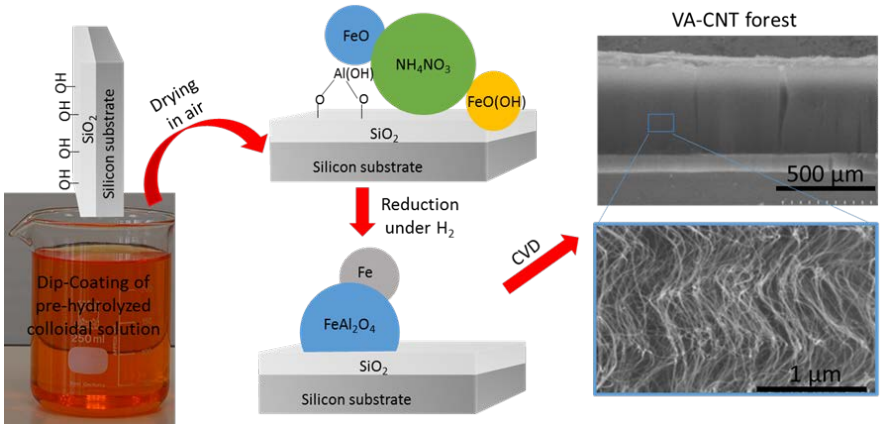

A simple and inexpensive route of large-scale elaboration of VA-CNTs

1. Introduction

During the last 25 years, carbon nanotubes (CNTs) have raised a great interest due to their unique structural and physical properties. Vertically aligned CNTs (VA-CNTs) arrays in particular have shown great potential for many applications such as field emission [1, 2], energy storage [3, 4], gas sensors [5, 6], membranes [7, 8], structural composites [9, 10] or thermal interface [11, 12]. Methods to produce tall and high-quality arrays of VA-CNTs are now well established, especially using the water-assisted catalytic chemical vapor deposition (C-CVD) process, the so-called "super-growth" [13]. Industrial manufacturing of VA-CNTs is on the rise but their production costs remain high, which strongly hinders the commercialization and wide application of VA-CNT-based materials.

The growth process of VA-CNTs typically involves a carbon feedstock decomposed at high temperature on metal catalyst nanoparticles supported on an oxide layer, such as SiO_2 [14], MgO [15], or Al_2O_3 [13, 16], which acts as a buffer layer to prevent catalyst ripening and diffusion in the bulk of the support (usually a silicon wafer). To date, the best and standard catalyst system for growing dense and tall VA-CNTs is a thin Fe film (0.4-2 nm) supported on an Al_2O_3 underlayer (10-100 nm) [17]. Al_2O_3 is particularly efficient as its role is not limited to a simple diffusion barrier but is also believed to reduce hydrocarbon contamination of the surface in the presence of H_2O [18] and to stabilize the oxidation state of iron nanoparticles (Fe^{2+} and Fe^{3+}) [19], restricting iron mobility on the surface, and therefore nanoparticle sintering [20]. In most studies to date on VA-CNT growth, the buffer and catalyst layers are typically prepared by physical vapor deposition (PVD) [21]. Although PVD systems are widely used in the semiconductor industry, a less expensive and demanding process of catalyst deposition would be highly beneficial for the large-scale and continuous production of VA-CNT arrays [22]. Our work was therefore motivated by the need for a simpler and cheaper method of catalyst preparation for the large-scale industrial production of VA-CNTs. Methods of wet deposition of metal (Fe, Co, Ni,…) have already been reported on alumina or silica have been developed using metal salt solutions or metal colloid suspensions as starting materials. The as-made catalysts showed activities comparable to those of PVD-prepared catalysts [22-26]. Wet-deposition methods were also developed to prepare the Al_2O_3 underlayer [27-29]. For example, Wang *et al.* developed a fully wet procedure using boehmite nanoplates (γ-AlO(OH)) deposited on a silicon chip, which were converted in a 20-nm thick Al_2O_3 buffer layer by annealing at 750 °C in air. After deposition of a colloidal suspension of Fe_3O_4 nanoparticles, they obtained a catalyst yielding millimeter-thick VA-CNT arrays [30]. However, this approach remains

complex and requires several steps: i) preparation and purification of the boehmite solution, ii) deposition of the particles, iii) annealing to form an Al_2O_3 layer, iv) preparation and deposition of the Fe_2O_3 colloidal suspension. Our goal was therefore to build on the versatility of wet methods while developing a simpler and cheaper process than those previously reported.

Here, we report a simple and fully wet approach to prepare catalysts able to grow dense and tall VA-CNT arrays on oxidized silicon wafers. The main novelty is that the aluminum-based buffer layer and the catalyst nanoparticles at its surface are formed together in a single step. This method is based on the dip-coating of a single solution of a mixture of $Fe(NO_3)_3$, $Al(NO_3)_3$ and NH_4OH which are widely available and low-cost precursors. Although similar approaches were already tested in previous works, they did not yield tall VA-CNT arrays (< 50 µm) [31-33]. We show here that a careful optimization of the concentrations of the different species in the solution leads to a growth activity and a VA-CNT quality comparable to those obtained with typical PVD-made catalysts in the same growth conditions.

2. Experimental

2.1. Materials

$Fe(NO_3)_3.9H_2O$ (ACS Reagent, >98%), $Al(NO_3)_3.9H_2O$ (ACS Reagent, >98%), NH_4OH (5 M) were purchased from Sigma-Aldrich and used without further purification. He (99.995%), H_2 (99.9995%) and C_2H_4 (99.95%) were purchased from Linde Gas. Gas flow were controlled using Brooks GF80 mass flow controllers. Silicon wafers were thermally oxidized on both sides to reach a layer of 600 nm of SiO_2. For reference, PVD Al_2O_3 sublayers were prepared by depositing 20 nm of Al_2O_3 by radio-frequency non-reactive sputtering. For control experiments with PVD Fe, 1 nm of Fe was further evaporated on top of the Al_2O_3 layer. Just prior to dip-coating, thermally oxidized Si substrates (*ca.* 15x50 mm²) were washed by immersion into an active NH_4OH (5 M) / H_2O_2 (5 M) / H_2O mixture for 15 min and then thoroughly washed with H_2O. Substrates coated with Al_2O_3 were thoroughly washed with acetone, isopropanol and H_2O.

2.2. Solution and catalyst preparation

0.50 g of $Fe(NO_3)_3.9H_2O$ was added to a 100 mL solution of 0.025 M NH_4OH to yield a clear brown solution (Fe solution, Figure 1). Then, 0.46 g $Al(NO_3)_3.9H_2O$ was added to yield a transparent brown and acidic solution (pH ~ 4) hereafter called FeAl[X] solution with X being

the Fe/Al molar ratio in the solution. These solutions were then dip-coated at 20 $mm.min^{-1}$ in a humidity- and temperature-controlled chamber (RH ≈ 50% at 27 °C) on freshly cleaned thermally oxidized silicon wafers. The samples were dried at room temperature for 1-24 h before CVD experiments.

2.3. VA-CNT growth

VA-CNT growth was performed using a standard water-assisted protocol [13]. Briefly, the samples were placed on top of a silicon sample holder (40x50 mm^2) in a 2-inches tubular furnace and heated in a He/H_2 mixture (600/400 sccm) during 15 min from room temperature to 750 °C. At 750 °C, 200 ppm of H_2O were added using a small flow of He in a water bubbler which was maintained at low temperature (typically 5 °C) and the samples were kept at 750 °C in this atmosphere for 5 min. Humidity was controlled using an hygrometer (MIS Probe 2, General Electrics) prior to each experiment. Then, the samples were exposed for 10 min to a He/C_2H_4 mixture (810/190 sccm) with 200 ppm H_2O to grow VA-CNTs. The furnace was then cooled under He at a temperature below 100 °C before opening and withdrawal of the samples to prevent VACNT oxidation.

The samples presented in this study were prepared in four different runs. During each run, a reference catalyst prepared by PVD with 1 nm of Fe on 20 nm of Al_2O_3 (**PVD: Fe@Al_2O_3**) was added in the furnace and the thickness of VACNT grown on it was controlled by an optical camera to confirm the reproducibility of the growth conditions independently of the environmental conditions.

2.4. Characterization

Scanning electron micrographs were obtained using a Hitachi S4800 operating at 10 kV. Raman characterization of the VA-CNTs was performed at a laser wavelength of 532 nm using a Horiba Jobin-Yvon T64000 spectrometer equipped with a silicon camera cooled with liquid nitrogen and a microscope. The focused laser spot on the sample was typically 1 µm. Atomic force micrographs were obtained using a Brucker AFM D3100 in tapping mode using a NCH point probe with a tip radius of 5 nm at F = 242.9 kHz, Q = 460 and k = 18 $N.m^{-1}$. X-Ray Photoelectron spectroscopy (XPS) measurements were performed on Mepitel®. The excitation source produced a monochromatic Al Kα line (1486.6 eV) and worked at 100 W of power. The analyzed surface had a 400-µm diameter. All XPS components were assigned from the analysis

of the values reported for reference compounds and referenced in the NIST database [34]. X-Ray diffraction (XRD) patterns were obtained using a PAN analytical X'Pert Pro MPD diffractometer at Cu Kα irradiation (λ = 1.5418 Å) with a step size of 0.033° (2θ scale) in the 12° - 80° interval. Note that in the case of powders submitted to a reducing treatment for subsequent XRD characterization, the samples were stored under inert gas just after the reducing treatment to prevent oxidation in air. For other samples, they were normally exposed to air as during the elaboration process before XRD and oxidation in air was taken into account for the XRD interpretation. Transmission Electron Microscopy (TEM) was first performed on a JEOL 1200 EX II operated at 100 kV. High-Resolution TEM (HRTEM) micrographs were obtained with a FEI Titan Cs image aberration-corrected microscope working at 80 kV. In the latter case, the observations were performed at low temperature (approx. 77 K) to avoid electron irradiation damage of the nanotubes and possible contamination of the samples. Micrographs were subsequently analyzed using the Gatan Digital Micrograph software taking intensity profiles through each tube to measure their diameter distribution.

3. Results

We first studied the influence of the catalyst preparation parameters on the features of the grown CNTs. Figure 1 shows the typical procedure for the experiments conducted throughout this study. First, we investigated the activity of a solution of $Fe(NO_3)_3$ in dilute NH_4OH (Fe solution). The role of NH_4OH is to allow the formation of metal hydroxides able to condense into nanoparticles. This solution was dip-coated on a thermally oxidized Si wafer (**Fe@SiO_2**) and on a silicon wafer coated with an extra layer of 20 nm of Al_2O_3 deposited by PVD (**Fe@Al_2O_3**). The activity of these catalysts was compared to that of a reference catalyst prepared by PVD with 1 nm of Fe on 20 nm of Al_2O_3 (**PVD: Fe@Al_2O_3**). In each run, the thickness of the VA-CNTs grown on the reference PVD catalyst was measured to be 660 µm +/- 10 %, thus confirming the good reproducibility of the growth conditions. We observed that thick VA-CNT arrays were grown on both **PVD:Fe@Al_2O_3** and **Fe@Al_2O_3**, with thickness of, respectively, 650 µm and 590 µm (Table 1, entries 1 and 2). At the opposite, a thin layer of entangled CNTs was grown with **Fe@SiO_2**, in good agreement with previous studies performed in the absence of an alumina under-layer [35, 36]. Second, we studied the influence of a PVD Al_2O_3 under-layer on the activity of the FeAl[X] catalysts. As shown in table 1 (entry 3), a **FeAl[1]** solution dip-coated on PVD Al_2O_3 (**FeAl[1]@Al_2O_3**) yielded a VA-CNT array with a thickness of 690 µm, while a slightly thinner array (550 µm) was obtained with the same

solution deposited on Si/SiO_2 (**FeAl[1]@SiO_2**, entry 7). Together, these results confirm the well-documented effect that an Al_2O_3 under-layer strongly promotes VA-CNT growth from Fe catalyst nanoparticles.

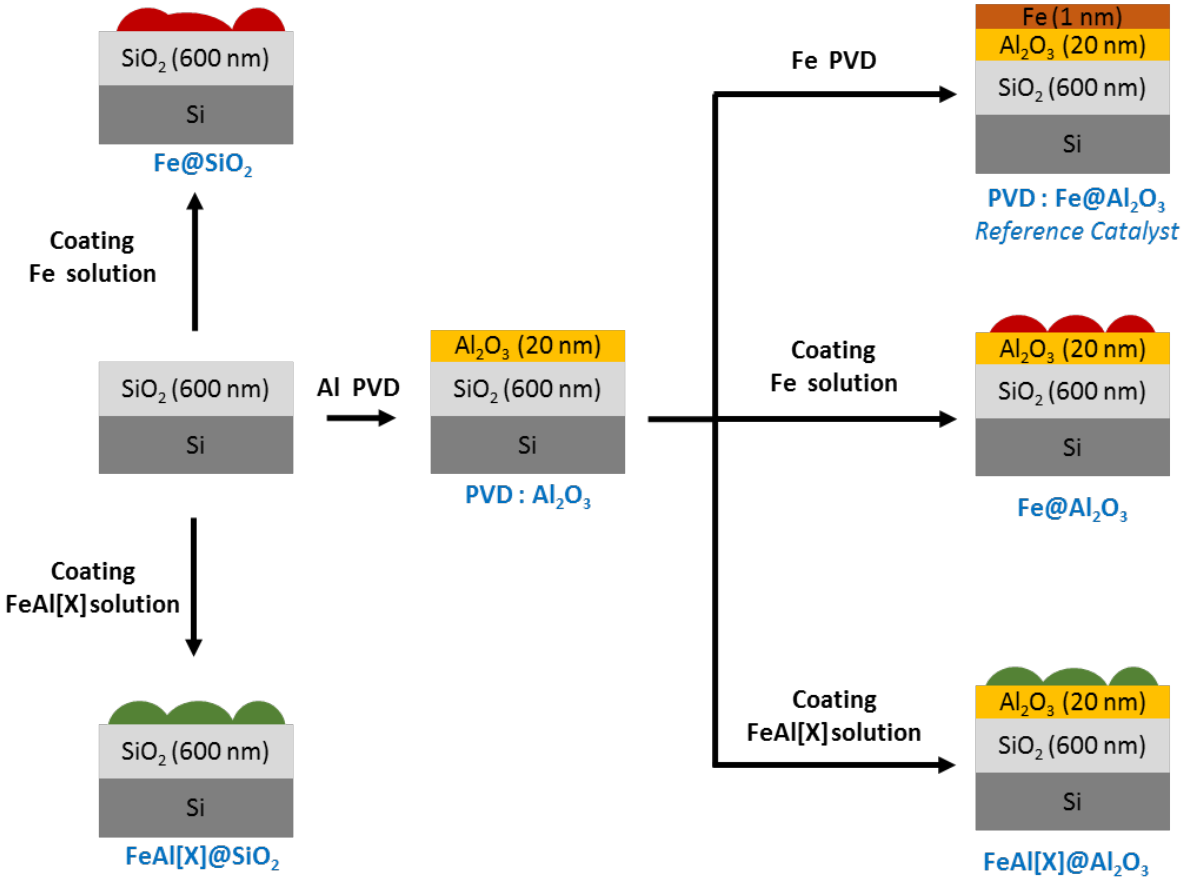

Figure 1. Protocols of catalyst preparation and corresponding catalyst nomenclature.

Third, we studied the influence of the Fe/Al ratio (X=[Fe]/[Al]) on the activity of the FeAl[X]@Al_2O_3 catalysts. The maximum VA-CNT thickness (660 µm) was obtained with a Fe/Al ratio of 0.6 (**FeAl[0.6]@SiO_2**, Table 1, entry 5). Importantly, this thickness is comparable to the one obtained with the reference PVD catalyst thus demonstrating that catalysts prepared by a simple dip-coating step can yield VA-CNT forests with heights similar to PVD-made catalysts. Higher and lower Fe/Al ratio yielded thinner VA-CNT layers (Table 1, entries 4-9). Fourth, the effect of increasing the total concentration of Fe and Al salts was investigated. By doubling the total concentration in Fe and Al salts, significantly taller VA-CNTs were obtained: 640 µm for **2xFeAl[1]@SiO_2** (entry 12) by comparison to 550 µm for **FeAl[1]@SiO_2** (entry 7). Note that for Fe solution deposited on PVD Al_2O_3, doubling the Fe concentration has little effect: 620 µm for **2xFe@Al_2O_3** (entry 10) to be compared to 590 µm for **Fe@Al_2O_3** (entry 2).

All together, these results highlight the high potential of this fully-wet single-step approach since a simple coating by Fe and Al salt solutions directly on Si/SiO_2 shows performances comparable to those of PVD catalysts.

The morphologies of the VA-CNT arrays were then analyzed by scanning electron microscopy (SEM) as shown in Figure 2. SEM pictures showed well aligned CNTs on all the samples grown on Al_2O_3 (Fig. 2a-c) while less aligned and curly CNTs were observed for the samples grown from **FeAl[X]@SiO$_2$** (Fig. 2d-h) with X between 0.2 and 1.5. Since alignment is essentially caused by steric interactions between CNTs, this supports that **FeAl[X]@SiO$_2$** catalysts yield a lower CNT density of the VACNT forests than PVD catalysts. In general, a lower homogeneity in CNT height was observed in VA-CNTs grown from **FeAl[X]@SiO$_2$** catalysts when compared to PVD catalysts, which also points toward a less homogeneous and less dense distribution of active catalyst particles.

Table 1. VA-CNT height, Raman G-band positions and G/D ratio (λ = 532 nm) of the samples grown from the different catalysts.

Entry	Catalyst	[Fe] (mol.L^{-1})	[Fe]/[Al]	VA-CNT height (µm)	G band (cm^{-1})	G/D ratio
1	**PVD: Fe@Al$_2$O$_3$**	N/A	N/A	660 +/- 10%	1584	3.2
2	**Fe@Al$_2$O$_3$**	0.0125	N/A	590	1583	2.2
3	**FeAl[1]@Al$_2$O$_3$**	0.0125	1	690	1581	3.7
4	**FeAl[0.2]@SiO$_2$**	0.0125	0.2	420	1576	1.1
5	**FeAl[0.6]@SiO$_2$**	0.0125	0.6	660	1576	1.2
6	**FeAl[0.8]@SiO$_2$**	0.0125	0.8	550	1578	2.8
7	**FeAl[1]@SiO$_2$**	0.0125	1	550	1579	1.5
8	**FeAl[1.5]@SiO$_2$**	0.0125	1.5	450	1584	1.5
9	**FeAl[2]@SiO$_2$**	0.0125	2	250	1577	1.2
10	**2xFe@Al$_2$O$_3$**	0.25	N/A	620	1575	4.8
11	**2xFeAl[0.8]@SiO$_2$**	0.25	0.8	n.d.	1580	2.5
12	**2xFeAl[1]@SiO$_2$**	0.25	1	640	1580	3.1

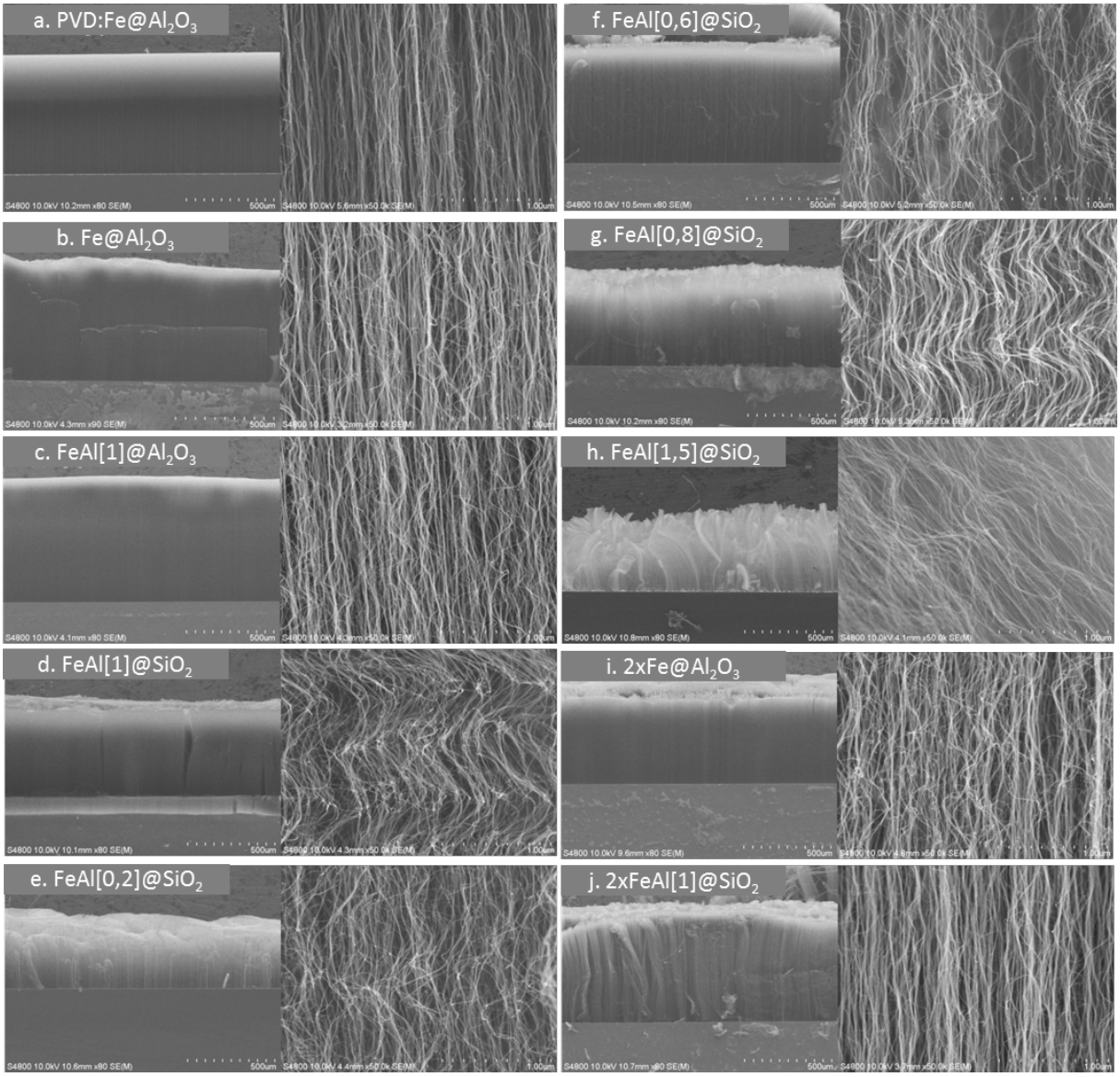

Figure 2. SEM pictures of the VA-CNTs grown from: a. PVD: Fe@Al_2O_3, b. Fe@Al_2O_3, c. FeAl[1]@Al_2O_3, d. FeAl[1]@SiO_2, e. FeAl[0.2]@SiO_2, f. FeAl[0.6]@SiO_2, g. FeAl[0.8]@SiO_2, h. FeAl[1.5]@SiO_2 , i. 2xFe@ Al_2O_3, j. 2xFeAl[1]@SiO_2.

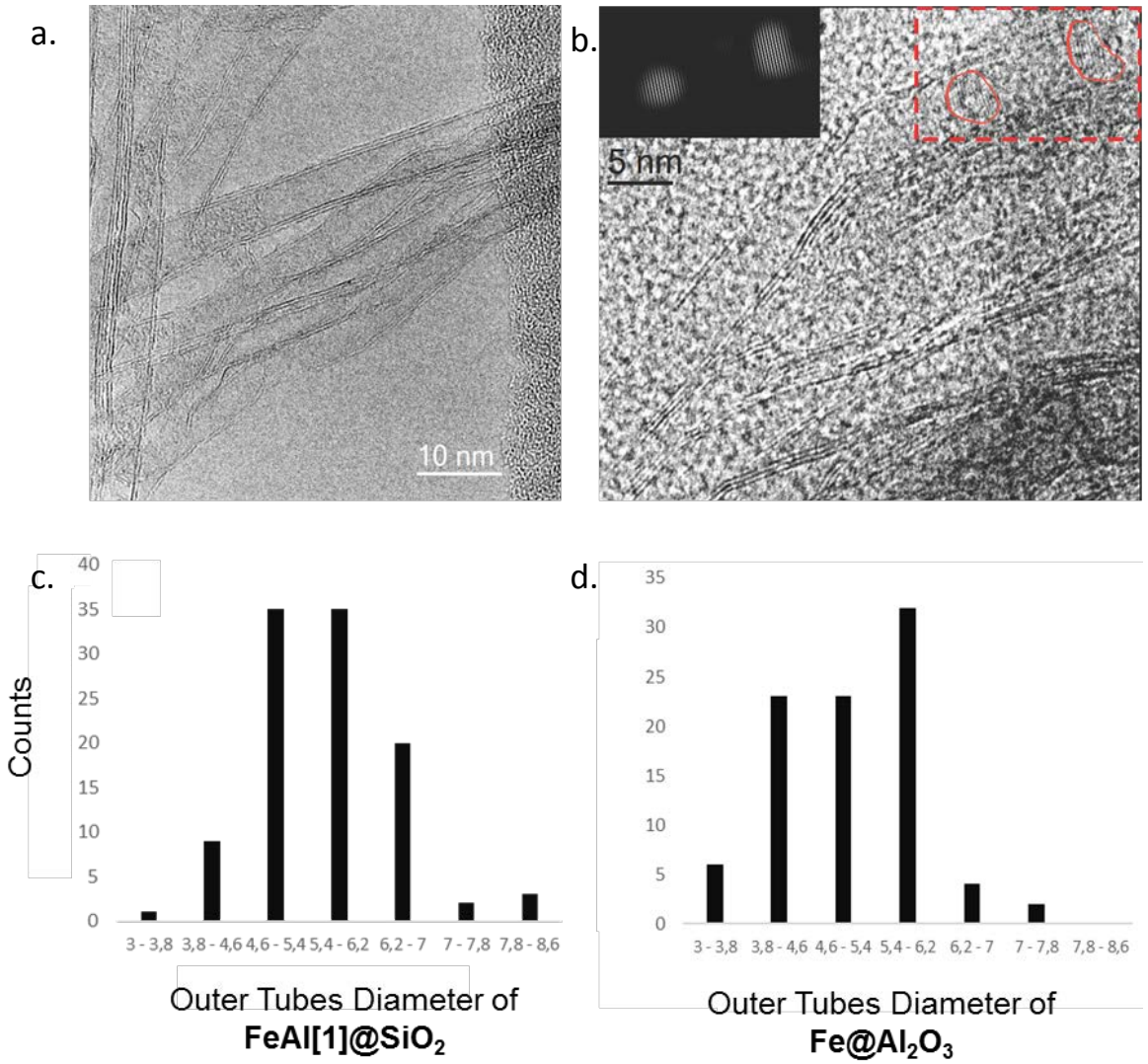

Figure 3. a,b) Representative HRTEM pictures of CNTs and catalyst crystalline nanoparticles (highlighted by a red contour) after growth using the FeAl[1]@SiO_2 catalyst. In b), a Fast Fourier Transform (FFT) has been applied to the TEM image and the crystalline spots corresponding to the catalyst NPs have been selected to apply an inverse FFT for building the insert image at the top left. c,d) Outer tubes diameter distribution diagram of FeAl[1]@SiO_2 (c) and Fe@Al_2O_3 (d), respectively.

The diameter distribution of the CNTs grown from **PVD: Fe@Al_2O_3**, **Fe@Al_2O_3**, and **FeAl[1]@SiO_2** were evaluated by TEM and found to be comparable for the three samples with most tubes having diameters of 5 +/- 1 nm. The structure of the CNTs grown from **FeAl[1]@SiO_2** was further analyzed by high-resolution TEM showing that mainly double- and triple-wall CNTs were obtained (Figure 3, mean size 5.6 +/- 1.6 nm with a ratio of 2.4 DWCNTs for 1 TWCNT). By comparison, VA-CNTs grown from **Fe@Al_2O_3** showed slightly thinner nanotubes with a higher proportion of DWCNTs (5.2 +/- 0.8 nm with 3.3 DWCNTs for 1

TWCNT, Figure 3). The crystalline quality of all CNTs was found relatively good and comparable to that reported in the literature for VA-CNTs grown from PVD-made catalysts.

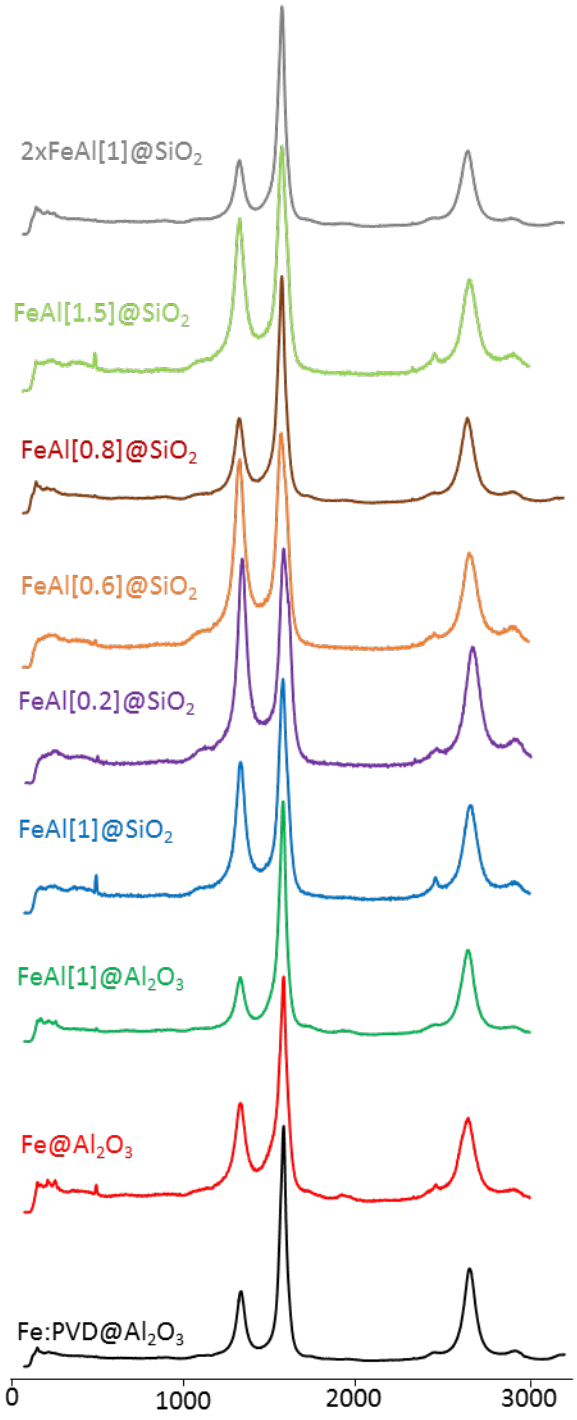

Figure 4. Raman spectra of VA-CNT arrays grown from the different catalysts.

The samples were then analyzed by micro-Raman spectroscopy (Figure 4). All the VA-CNTs samples showed a G band at around 1580 cm^{-1} (see Table 1) as expected from a sample

dominated by multi-walled CNTs (MWCNTs) with diameters in the range of 3-7 nm as measured by HRTEM (Figure 3). All samples also displayed D and 2D (G') bands at positions in the range of 1327-1338 cm^{-1} and 2642-2670 cm^{-1}, respectively. This is also in good agreement with the positions expected for MWCNTs at 532 nm of laser excitation. Many samples showed additional signals at low frequencies (less than 280 cm^{-1}) associated with the radial breathing modes (RBMs) of small diameter CNTs (d = 1-3 nm). The occurrence of RBMs is systematically associated with higher intensities of the G and 2D bands and to downshifted D and 2D bands as also expected when moving toward such smaller-diameter CNTs. Since CNTs of 1-3 nm were not observed during our HRTEM observations but display an intrinsically higher Raman cross section due to the resonance effect, the results agree with samples mainly composed of double/triple-wall CNTs with 3-7 nm diameter with traces of CNTs with 1-3 nm diameter. The proportion of small-diameter CNTs was generally found higher for the catalysts deposited on PVD alumina. Note that having a mixture of large-diameter CNTs (weakly resonant and with low G/D ratio) and small-diameter CNT (highly resonant and with high G/D ratio) hinders the use of the G/D ratio (Table 1) to evaluate the overall crystalline purity of the sample. Instead, for the samples studied here, a higher G/D ratio essentially denotes a higher proportion of small-diameter CNTs in agreement with the other Raman features (more intense RBMs, downshifted D and 2D bands). By comparing the Raman spectra at different positions, one may roughly estimate that large- and small-diameter CNTs display a G/D ratio in the range of 1-2 and 2-6, respectively and quite independently of the catalyst. Of course, this value is expected to strongly vary with the growth conditions (temperature, precursor pressure) used [37]. Overall, the TEM and Raman results shows that our wet-based catalyst preparation method allows the preparation of VA-CNT arrays with similar morphology and structural quality than standard PVD catalyst, yet with the use of simpler protocol and laboratory equipment.

4. Discussion

To understand the effect of the addition of the Al salt, the catalyst formation mechanism was investigated using Atomic Force Microscopy (AFM), X-ray Diffraction (XRD) and X-ray Photoelectron Spectroscopy (XPS).

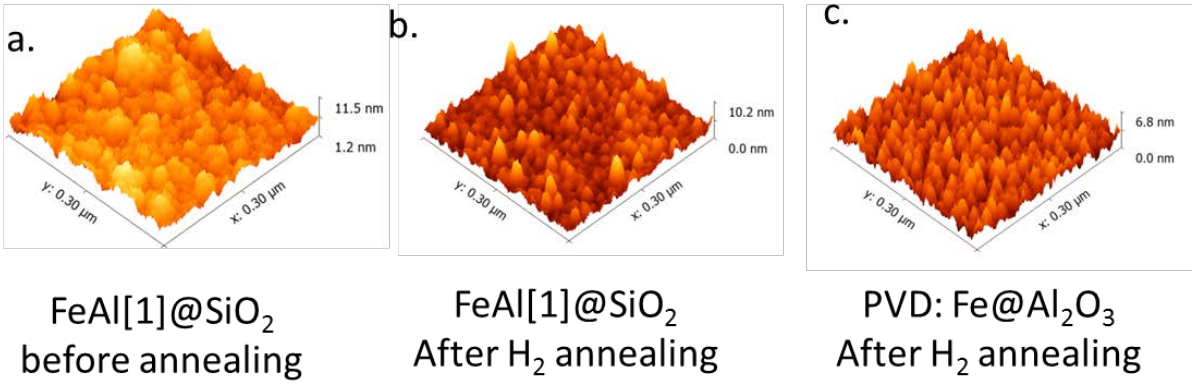

Figure 5. AFM images of a. FeAl[1]@SiO_2 before annealing, b. FeAl[1]@SiO_2 after annealing at 750 °C under H_2 and c. PVD: Fe@Al_2O_3 after annealing at 750 °C under H_2.

AFM observations of the samples after deposition of solution FeAl[1] on Si/SiO_2 and drying were first performed. As shown in Figure 5a, large nanoparticle aggregates of 10-50 nm were observed on the surface. Since the diameter of a MWCNT is strongly related to the size of its catalyst particle [36, 38], these particles are not likely to be directly responsible for the observed catalytic activity since the CNT diameter distribution was determined to be 5.6 +/- 1.6 nm (Figure 3c). Interestingly, after annealing at 750°C under a He/H_2 mixture with 200 ppm H_2O and rapid cooling to RT under a He/H_2 flow, well-defined and smaller nanoparticles were observed (height around 5 nm) on the surface (Figure 5b). When compared to the PVD catalyst (Figure 5c) whose surface is very homogeneous after reduction, **FeAl[1]@SiO_2** surface shows the presence of some larger nanoparticles (around 10 nm in height). This is in good agreement with our SEM observations of less dense and curvy VA-CNTs [39] obtained with the catalysts prepared by dip-coating. From AFM measurements, it is clear that a severe surface reconstruction occurs during the H_2 treatment.

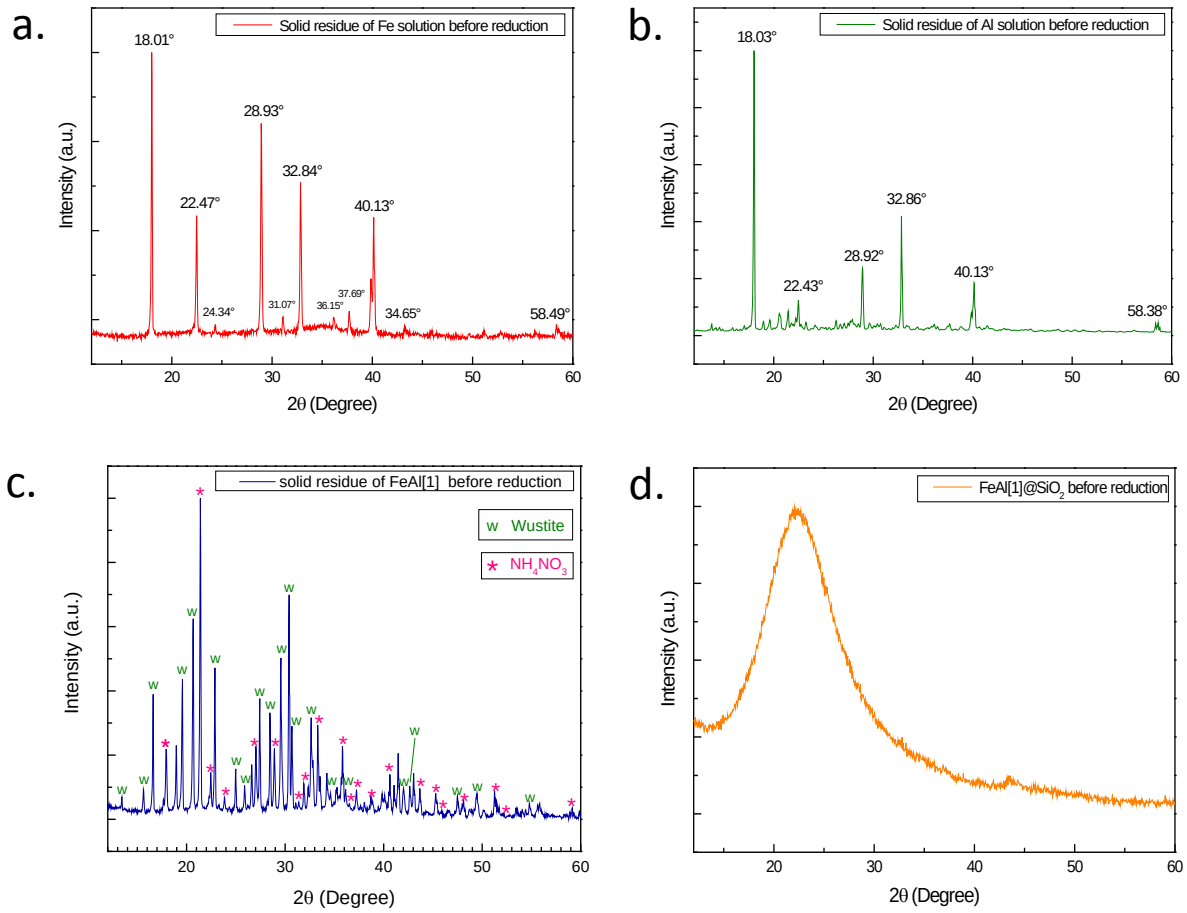

Figure 6. a. XRD of the dry residue of $Fe(NO_3)_3$ aqueous solution with 1 equivalent of NH_4OH before reduction showing mainly the presence of NH_4NO_3 [40] (ICSD collection code 002772). b. XRD of the dry residue of a $Al(NO_3)_3$ aqueous solution with 1 equivalent of NH_4OH before reduction showing mainly the presence of NH_4NO_3 [40] c. XRD of a dry residue of a FeAl[1] solution showing mainly the presence of Wuestite (Iron Oxide $Fe_{0.902}O$) [41] (ICSD collection code 040089) and NH_4NO_3 [40]. d. XRD of FeAl[1] impregnated on high surface area silica solution after reduction under H_2 at 750°C showing only the typical large shoulder of amorphous silica.

To further investigate the composition of the thin catalyst film before CVD experiments, XRD measurements of the solid residue obtained after evaporation of the different solutions were performed. Before reduction, the solid residue of a $Fe(NO_3)_3$ aqueous solution with 1 equivalent of NH_4OH (Fe solution) showed the presence of crystalline NH_4NO_3 (Figure 6a) with average crystal sizes larger than 100 nm. The same result was obtained for the solid residue of a $Al(NO_3)_3$ aqueous solution with 1 equivalent of NH_4OH (Figure 6b). The residue of **FeAl[1]** also showed the presence of crystalline NH_4NO_3 nanoparticles, along with crystalline FeO nanoparticles (Figure 6c). However, there was no signature of crystalline Al-based compounds.

Interestingly, when solution **FeAl[1]** was coated on high surface-area silica and reduced under H_2, no diffraction peaks were observed, which indicates that large metallic Fe nanoparticles were not formed in agreement with AFM observations (Figure 6d). The disappearance of the large NH_4NO_3 crystal nanoparticles previously observed provides an explanation for the evolution of surface roughness observed by AFM before and after H_2 reduction as further supported by the decomposition temperature of NH_4NO_3 (210°C).

XPS analysis were then performed. Surface analysis of sample **FeAl[1]@SiO_2** after drying, but before reduction under H_2, showed a very large contribution of the SiO_2 substrate with 25.5% of Si, and only 5.0% of Al and 5.0% of Fe (Table 2).

Table 2. Surface composition of the catalyst: elemental composition from XPS.

Sample Name	Treatment	Si (2p)	O (1s)	Fe (2p)	Al (2p)
FeAl[1]@SiO_2	after deposition	25.7	64.2	5.1	5.1
FeAl[1]@SiO_2	after H_2 reduction	36.7	58.3	1.2	3.7
Fe@SiO_2	after H_2 reduction	41.1	58.4	0.5	0,0
Fe@Al_2O_3	after H_2 reduction	0,0	55.8	1.0	43.1

Since XPS is only sensitive to the top 10 nm of the surface, this indicates that the deposited layer is very thin (less than 10 nm) and/or not continuous. The Fe $2p_{3/2}$ profile is made of two contributions: an Fe(II) contribution at 709.8 eV and an Fe(III) contribution at 711.1 eV with a Fe(II)/Fe(III) ratio of 1.65, plus two satellite peaks at higher energy (Figure 7a) . This excludes the presence of metallic iron (expected at ~707 eV), of iron silicide (Fe_3Si expected at 707.5 eV) and of iron silicate (Fe_2SiO_4 expected at 708.9-709.0 eV). It also excludes the possibility of a single Fe(II) or Fe(III) compound, or of Fe_3O_4 only (which has an Fe(II)/Fe(III) ratio of 0.5). For the Fe(III) peak at 711.1 eV, the most likely assignment is FeO(OH) (expected at 711.0-711.8 eV) or alternatively Fe_2O_3 (which is expected at 710.7-711.4 eV). For the Fe(II) peak at 709.8 eV, the most likely assignment is FeO which is expected at 709.6-710.3 eV. The Al 2p peak is found at 74.8 eV (Figure 7c) which would nicely agree with an aluminosilicate such as Al_2OSiO_4 (expected at 74.5-74.9 eV) or an aluminum silicate hydroxide such as $Al_2Si_4O_{10}(OH)_2$ (expected at ~74.7 eV), which in both cases would support a strong anchoring of aluminum with the SiO_2 substrate.

After H_2 annealing, an even larger atomic contribution of Si (36.6 %) was observed, with 3.7% of Al and 1.2% of Fe remaining on the surface (Table 2), showing significant Fe diffusion in the SiO_2 matrix at high temperature (750°C). The Fe $2p_{3/2}$ profile displayed little change with still two contributions: an Fe(II) contribution at 710.1 eV and an Fe(III) contribution at 711.4 eV with about the same Fe(II)/Fe(III) ratio as before reduction (Figure 7b). At the opposite, the Al 2p peak was strongly downshifted to 74.0 eV (Figure 7c), which could be assigned to $Al(OH)_3$ (expected at 73.9-74.4 eV) or alternatively to $FeAl_2O_4$ (expected at ~74.3 eV). The latter one should give rise to an Fe $2p_{3/2}$ contribution at ~710.0 eV which is in good agreement with the Fe(II) peak observed at 710.1 eV. We performed the same H_2 treatment and XPS analysis on the same solution without $Al(NO_4)_3$ (*i.e.* **Fe@SiO$_2$**) and found that the amount of Fe remaining at the surface was about three times less (Table 2). This provides an additional support for the formation of an iron aluminate such as $FeAl_2O_4$ which would stabilize Fe at the surface of SiO_2. The remaining Fe(III) peak is assigned to Fe_2O_3 and/or FeO(OH) formed from reduced iron when exposed to air (Figure 7d).

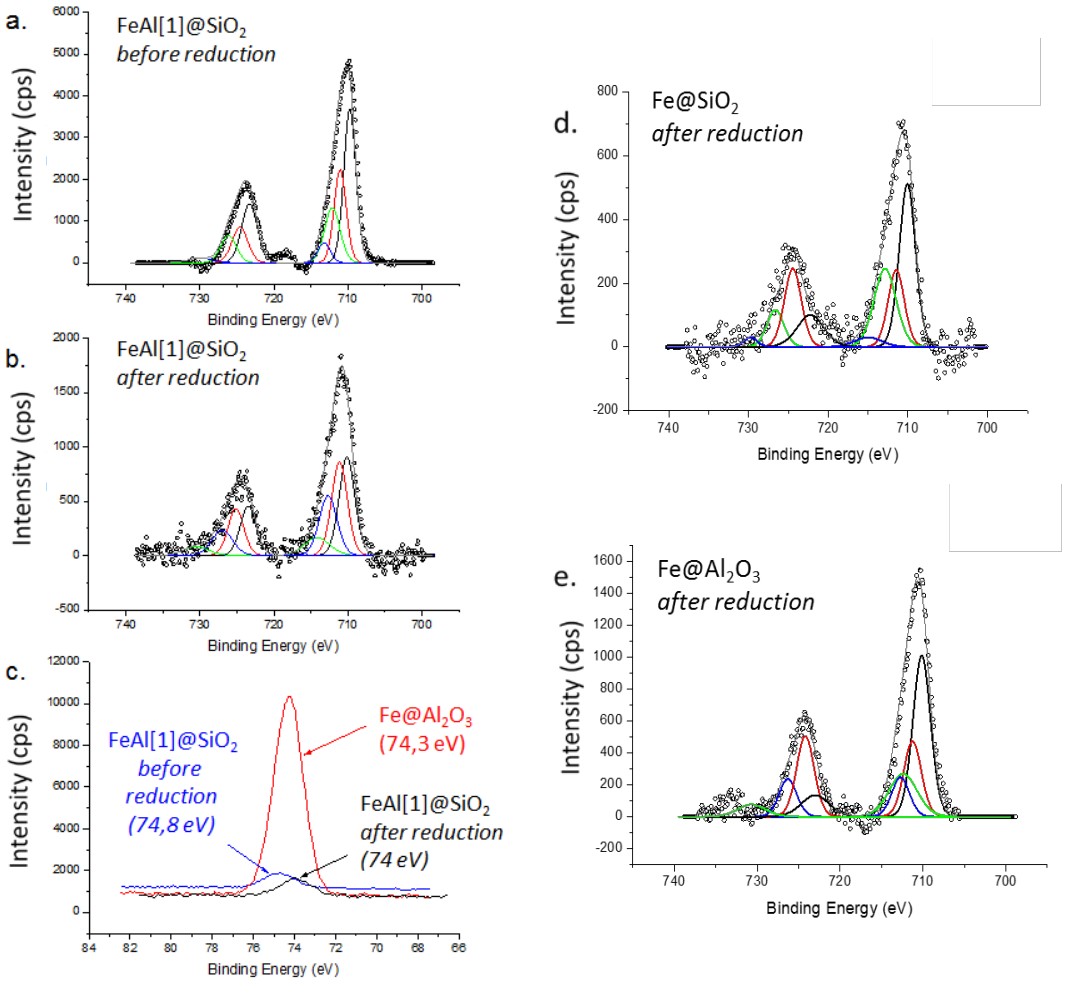

Figure 7. Fe 2p XPS spectra of a) FeAl[1]@SiO_2 before H_2 reduction, and b) after H_2 reduction; c) Al 2p XPS spectra of FeAl[1]@SiO_2 before H_2 reduction (blue), and after H_2 reduction (black) compared to Fe@Al_2O_3 after H_2 reduction (red); Fe 2p XPS spectra of d) Fe@SiO_2 after H_2 reduction and e) Fe@Al_2O_3 after H_2 reduction.

Taken together, these results support the following picture (Figure 8). During air drying, $Al(OH)_3$ tends to react with the SiO_2 surface (*e.g.* with hydroxyl groups) to form a surface layer of aluminosilicate or aluminum silicate hydroxide compounds, while $Fe(OH)_3$ tends to form FeO or FeO(OH) nanoparticles. During H_2 annealing, particles of Fe oxides and hydroxides can either get reduced to metallic iron which then tends to diffuse into the SiO_2 substrate. Alternatively, in the presence of surface aluminum oxides or hydroxides, they can form surface layers of iron aluminates which are less reducible and act as a buffer layer which stabilizes small iron nanoparticles at their surface. So, beside its standard role of diffusion barrier, SiO_2

plays another role in our process, by allowing the formation of a mixed Al-Si oxidized layer which will anchor and stabilize catalyst nanoparticles. If exposed to a carbon source during CVD, these stabilized iron particles will allow the growth of long CNTs. Instead, if exposed to air, these iron nanoparticles will quickly become oxidized into Fe(III) compounds such as Fe_2O_3 or FeO(OH). This mechanism supports that increasing the concentration of Al in the solution at constant ratio with Fe should increase the surface coverage with aluminum compounds and therefore a higher density of stabilized iron particles and so a higher yield of long and defective nanotubes: this is in perfect line with our previous observation that doubling the proportion of Fe and Al promotes both a taller VACNT forest and a lower defect density (see entry 12 of table 1).

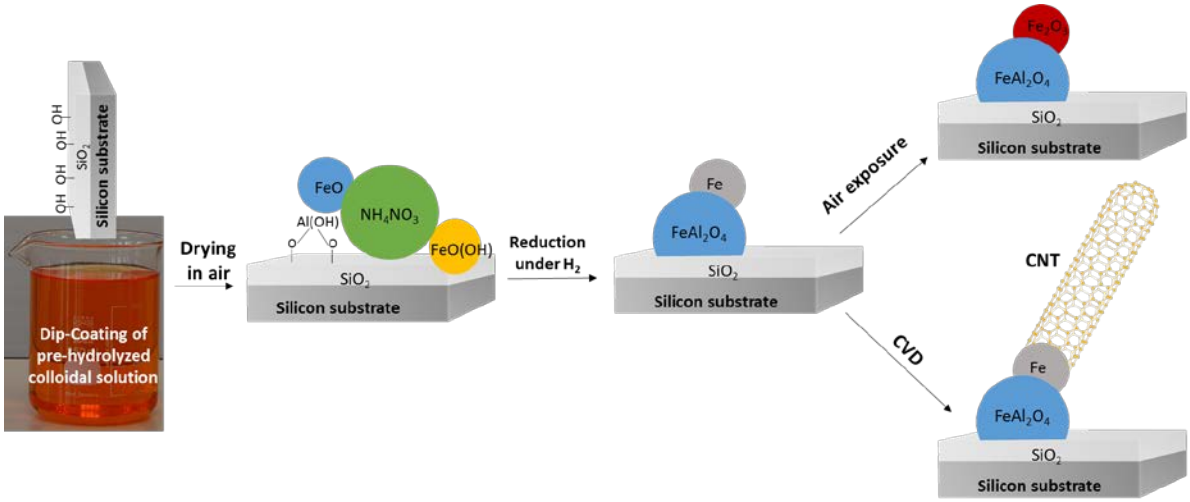

Figure 8. Proposed mechanism for catalyst formation and evolution.

5. Conclusion

In this study, a fully wet process was developed to prepare, in a single deposition step, a catalyst to grow VA-CNT arrays on standard SiO_2/Si wafers. This is important from a materials engineering point of view because the process is much simpler and cheaper than existing preparation methods. We therefore expect it to be easily transferred to industry for low-cost and large-area coating of catalyst for VA-CNT growth. This catalyst, prepared from a mixture of $Fe(NO_3)_3$ and an $Al(NO_3)_3$, yields VACNT height comparable to those of Fe/Al_2O_3 catalysts prepared by PVD which is standardly used for VA-CNT growth. Our study showed that, when mixed together, aluminum hydroxides preferentially react with the SiO_2 surface while iron

hydroxides tend to react together to form oxide or hydroxide nanoparticles: this explains why a single solution step can be used to prepare both an aluminum-based buffer layer and catalyst nanoparticles at its surface. This is important from a materials science point of view because it shows that chemical affinities between reactants can be played with to elaborate the catalyst nanoparticles and their supporting layer together in a single step. Following this initial demonstration, the approach may be further optimized and generalized to other catalysts to increase the homogeneity and density of the CNT forest and obtain a better control of the CNT diameter and crystalline quality. This simple and versatile approach appears as a strong alternative to PVD to easily prepare VA-CNT forests on various substrates, such as curved, porous or conducting substrates. Importantly for applications in electronics and electrochemistry requiring to electrically contact VA-CNT arrays, this process requires only a very thin layer of insulating oxide material, therefore allowing a more intimate contact between CNTs and their substrate.

Acknowledgement

We thank Michel Ramonda and the Near-Field Microscopy service (CTM) of the University of Montpellier for AFM analyses. HRTEM studies were conducted at the Laboratorio de Microscopias Avanzadas, Instituto de Nanociencia de Aragon, Universidad de Zaragoza, Spain. The Government of Aragon, and the European Social Fund are gratefully acknowledged. R.A. gratefully acknowledges the project “Construyendo Europa desde Aragon” 2014-2020 (grant number E/26). R.A. gratefully acknowledges the support from the Spanish Ministry of Economy and Competitiveness (MINECO) through project grant MAT2016-79776-P (AEI/FEDER, UE). Part of this work has received funding from the European Union’s Horizon 2020 research and innovation program under the Marie Sklodowska-Curie grant agreement No 642742.

Data availability

No raw/processed data are required to reproduce these findings.

References

[1] W.A. de Heer, A. Châtelain, D. Ugarte, A Carbon Nanotube Field-Emission Electron Source, Science. 270 (1995) 1179-1180. https://doi.org/10.1126/science.270.5239.1179

[2] N. Perea-López, B. Rebollo-Plata, J.A. Briones-León, A. Morelos-Gómez, D. Hernández-Cruz, G.A. Hirata, V. Meunier, A.R. Botello-Méndez, J.-C. Charlier, B. Maruyama, E. Muñoz-Sandoval, F. López-Urías, M. Terrones, H. Terrones, Millimeter-Long Carbon Nanotubes: Outstanding Electron-Emitting Sources, ACS Nano. 5 (2011) 5072-5077. https://doi.org/10.1021/nn201149y
[3] D.N. Futaba, K. Hata, T. Yamada, T. Hiraoka, Y. Hayamizu, Y. Kakudate, O. Tanaike, H. Hatori, M. Yumura, S. Iijima, Shape-engineerable and highly densely packed single-walled carbon nanotubes and their application as super-capacitor electrodes, Nat Mater. 5 (2006) 987-994. https://doi.org/10.1038/nmat1782
[4] K. Byungwoo, C. Haegeun, K. Woong, High-performance supercapacitors based on vertically aligned carbon nanotubes and nonaqueous electrolytes, Nanotechnology. 23 (2012) 155401. https://doi.org/10.1088/0957-4484/23/15/155401
[5] Y. Wang, J.T.W. Yeow, A Review of Carbon Nanotubes-Based Gas Sensors, Journal of Sensors. 2009 (2009) 24. https://doi.org/10.1155/2009/493904
[6] D.R. Kauffman, A. Star, Carbon Nanotube Gas and Vapor Sensors, Angewandte Chemie International Edition. 47 (2008) 6550-6570. https://doi.org/10.1002/anie.200704488
[7] B.J. Hinds, N. Chopra, T. Rantell, R. Andrews, V. Gavalas, L.G. Bachas, Aligned Multiwalled Carbon Nanotube Membranes, Science. 303 (2004) 62-65. https://doi.org/10.1126/science.1092048
[8] F. Du, L. Qu, Z. Xia, L. Feng, L. Dai, Membranes of Vertically Aligned Superlong Carbon Nanotubes, Langmuir. 27 (2011) 8437-8443. https://doi.org/10.1021/la200995r
[9] H. Cebeci, R.G.d. Villoria, A.J. Hart, B.L. Wardle, Multifunctional properties of high volume fraction aligned carbon nanotube polymer composites with controlled morphology, Composites Science and Technology. 69 (2009) 2649-2656. https://doi.org/10.1016/j.compscitech.2009.08.006
[10] V.P. Veedu, A. Cao, X. Li, K. Ma, C. Soldano, S. Kar, P.M. Ajayan, M.N. Ghasemi-Nejhad, Multifunctional composites using reinforced laminae with carbon-nanotube forests, Nat Mater. 5 (2006) 457-462. https://doi.org/10.1038/nmat1650
[11] T. Tong, Y. Zhao, L. Delzeit, A. Kashani, M. Meyyappan, A. Majumdar, Dense vertically aligned multiwalled carbon nanotube arrays as thermal interface materials, IEEE Transactions on Components and Packaging Technologies. 30 (2007) 92. https://doi.org/10.1109/TCAPT.2007.892079
[12] J. Liu, T. Wang, Y. Fu, L. Ye, Use of carbon nanotubes in potential electronics packaging applications, in 10th IEEE International Conference on Nanotechnology (IEEE-NANO), Seoul, South Korea, IEEE, 2010, 160-166. https://doi.org/10.1109/NANO.2010.5698052
[13] K. Hata, D.N. Futaba, K. Mizuno, T. Namai, M. Yumura, S. Iijima, Water-Assisted Highly Efficient Synthesis of Impurity-Free Single-Walled Carbon Nanotubes, Science. 306 (2004) 1362-1364. https://doi.org/10.1126/science.1104962
[14] S. Maruyama, E. Einarsson, Y. Murakami, T. Edamura, Growth process of vertically aligned single-walled carbon nanotubes, Chemical Physics Letters. 403 (2005) 320-323. https://doi.org/10.1016/j.cplett.2005.01.031
[15] G.-Y. Xiong, D.Z. Wang, Z.F. Ren, Aligned millimeter-long carbon nanotube arrays grown on single crystal magnesia, Carbon. 44 (2006) 969-973. https://doi.org/10.1016/j.carbon.2005.10.015
[16] S. Esconjauregui, M. Fouquet, B.C. Bayer, C. Ducati, R. Smajda, S. Hofmann, J. Robertson, Growth of ultrahigh density vertically aligned carbon nanotube forests for interconnects, ACS Nano. 4 (2010) 7431-7436. https://doi.org/10.1021/nn1025675
[17] S.P. Patole, P.S. Alegaonkar, H.-C. Lee, J.-B. Yoo, Optimization of water assisted chemical vapor deposition parameters for super growth of carbon nanotubes, Carbon. 46 (2008) 1987-1993. https://doi.org/10.1016/j.carbon.2008.08.009

[18] N. Suguru, H. Kei, S. Hisashi, K. Kazunori, Z. Zhengyi, M. Shigeo, Y. Yukio, Millimeter-Thick Single-Walled Carbon Nanotube Forests: Hidden Role of Catalyst Support, Japanese Journal of Applied Physics. 46 (2007) L399. https://doi.org/10.1143/JJAP.46.L399
[19] C. Mattevi, C.T. Wirth, S. Hofmann, R. Blume, M. Cantoro, C. Ducati, C. Cepek, A. Knop-Gericke, S. Milne, C. Castellarin-Cudia, S. Dolafi, A. Goldoni, R. Schloegl, J. Robertson, In-situ X-ray Photoelectron Spectroscopy Study of Catalyst−Support Interactions and Growth of Carbon Nanotube Forests, The Journal of Physical Chemistry C. 112 (2008) 12207-12213. https://doi.org/10.1021/jp802474g
[20] P.B. Amama, C.L. Pint, S.M. Kim, L. McJilton, K.G. Eyink, E.A. Stach, R.H. Hauge, B. Maruyama, Influence of Alumina Type on the Evolution and Activity of Alumina-Supported Fe Catalysts in Single-Walled Carbon Nanotube Carpet Growth, ACS Nano. 4 (2010) 895-904. https://doi.org/10.1021/nn901700u
[21] S. Yasuda, D.N. Futaba, T. Yamada, J. Satou, A. Shibuya, H. Takai, K. Arakawa, M. Yumura, K. Hata, Improved and Large Area Single-Walled Carbon Nanotube Forest Growth by Controlling the Gas Flow Direction, ACS Nano. 3 (2009) 4164-4170. https://doi.org/10.1021/nn9007302
[22] S. Sakurai, H. Nishino, D.N. Futaba, S. Yasuda, T. Yamada, A. Maigne, Y. Matsuo, E. Nakamura, M. Yumura, K. Hata, Role of Subsurface Diffusion and Ostwald Ripening in Catalyst Formation for Single-Walled Carbon Nanotube Forest Growth, Journal of the American Chemical Society. 134 (2012) 2148-2153. https://doi.org/10.1021/ja208706c
[23] J.D. Beard, J. Stringer, O.R. Ghita, P.J. Smith, High Yield Growth of Patterned Vertically Aligned Carbon Nanotubes Using Inkjet-Printed Catalyst, ACS Applied Materials & Interfaces. 5 (2013) 9785-9790. https://doi.org/10.1021/am402942q
[24] K. Mizuno, K. Hata, T. Saito, S. Ohshima, M. Yumura, S. Iijima, Selective Matching of Catalyst Element and Carbon Source in Single-Walled Carbon Nanotube Synthesis on Silicon Substrates, The Journal of Physical Chemistry B. 109 (2005) 2632-2637. https://doi.org/10.1021/jp0454117
[25] H. Nishino, S. Yasuda, T. Namai, D.N. Futaba, T. Yamada, M. Yumura, S. Iijima, K. Hata, Water-Assisted Highly Efficient Synthesis of Single-Walled Carbon Nanotubes Forests from Colloidal Nanoparticle Catalysts, The Journal of Physical Chemistry C. 111 (2007) 17961-17965. https://doi.org/10.1021/jp0723719
[26] E.S. Polsen, M. Bedewy, A.J. Hart, Decoupled Control of Carbon Nanotube Forest Density and Diameter by Continuous-Feed Convective Assembly of Catalyst Particles, Small. 9 (2013) 2564-2575. https://doi.org/10.1002/smll.201202878
[27] S. Dörfler, A. Meier, S. Thieme, P. Németh, H. Althues, S. Kaskel, Wet-chemical catalyst deposition for scalable synthesis of vertical aligned carbon nanotubes on metal substrates, Chemical Physics Letters. 511 (2011) 288-293. https://doi.org/10.1016/j.cplett.2011.06.027
[28] H. Wang, C. Na, Chemical Bath Deposition of Aluminum Oxide Buffer on Curved Surfaces for Growing Aligned Carbon Nanotube Arrays, Langmuir. 31 (2015) 7401-7409. https://doi.org/10.1021/acs.langmuir.5b01002
[29] N.T. Alvarez, C.E. Hamilton, C.L. Pint, A. Orbaek, J. Yao, A.L. Frosinini, A.R. Barron, J.M. Tour, R.H. Hauge, Wet Catalyst-Support Films for Production of Vertically Aligned Carbon Nanotubes, ACS Applied Materials & Interfaces. 2 (2010) 1851-1856. https://doi.org/10.1021/am100128m
[30] H. Wang, C. Na, Synthesis of millimeter-long vertically aligned carbon nanotube arrays on aluminum oxide buffer prepared by layer-by-layer assembly of boehmite nanoplates, Carbon. 66 (2014) 727-729. https://doi.org/10.1016/j.carbon.2013.09.034

[31] J.-M. Bonard, P. Chauvin, C. Klinke, Monodisperse Multiwall Carbon Nanotubes Obtained with Ferritin as Catalyst, Nano Letters. 2 (2002) 665-667. https://doi.org/10.1021/nl0255606
[32] L.Q. Fei L, Jia QX, Luo HM, Polymer-Assisted Deposition of Composite Catalysts for the Growth of Vertical Aligned Carbon Nanotubes, Chem Eng Process Tech. 1 (2013) 1013.
[33] P.M. Parthangal, R.E. Cavicchi, M.R. Zachariah, A generic process of growing aligned carbon nanotube arrays on metals and metal alloys, Nanotechnology. 18 (2007) 185605. https://doi.org/10.1088/0957-4484/18/18/185605
[34] A. V. Naumkin, A. Kraut-Vass, S. W. Gaarenstroom, C. J. Powell, NIST X-ray Photoelectron Spectroscopy Database, NIST Standard Reference Database 20, Version 4.1, U.S. Secretary of Commerce, (2012). https://srdata.nist.gov/xps/
[35] P.B. Amama, C.L. Pint, F. Mirri, M. Pasquali, R.H. Hauge, B. Maruyama, Catalyst–support interactions and their influence in water-assisted carbon nanotube carpet growth, Carbon. 50 (2012) 2396-2406. https://doi.org/10.1016/j.carbon.2012.01.045
[36] A. Kaneko, K. Yamada, R. Kumahara, H. Kato, Y. Homma, Comparative Study of Catalytic Activity of Iron and Cobalt for Growing Carbon Nanotubes on Alumina and Silicon Oxide, The Journal of Physical Chemistry C. 116 (2012) 26060-26065. https://doi.org/10.1021/jp309232w
[37] M. Picher, H. Navas, R. Arenal, E. Quesnel, E. Anglaret, V. Jourdain, Influence of the growth conditions on the defect density of single-walled carbon nanotubes, Carbon. 50 (2012) 2407-2416. https://doi.org/10.1016/j.carbon.2012.01.055
[38] C.L. Cheung, A. Kurtz, H. Park, C.M. Lieber, Diameter-Controlled Synthesis of Carbon Nanotubes, The Journal of Physical Chemistry B. 106 (2002) 2429-2433. https://doi.org/10.1021/jp0142278
[39] Y. Zhang, G. Zou, S.K. Doorn, H. Htoon, L. Stan, M.E. Hawley, C.J. Sheehan, Y. Zhu, Q. Jia, Tailoring the Morphology of Carbon Nanotube Arrays: From Spinnable Forests to Undulating Foams, ACS Nano. 3 (2009) 2157-2162. https://doi.org/10.1021/nn9003988
[40] C.S. Choi, J.E. Mapes, E. Prince, The structure of ammonium nitrate (IV), Acta Crystallogr. B28 (1972) 1357-1361. https://doi.org/10.1107/S0567740872004303
[41] A. Yamamoto, Modulated structure of wustite (Fe1-xO) (three-dimensional modulation), Acta Crystallogr. B38 (1982) 1451-1456. https://doi.org/10.1107/S056774088200613X